Nano Research 2017, 10(4): 1434–1447
DOI 10.1007/s12274-017-1525-3
Research Article
ISSN 1998-0124
CN 11-5974/O4

Controlled growth and photoconductive properties of hexagonal SnS_2 nanoflakes with mesa-shaped atomic steps

Yi Hu[1], Tao Chen[1], Xiaoqi Wang[1], Lianbo Ma[1], Renpeng Chen[1], Hongfei Zhu[1], Xin Yuan[1], Changzeng Yan[1], Guoyin Zhu[1], Hongling Lv[1], Jia Liang[1], Zhong Jin[1] (✉), and Jie Liu[1,2] (✉)

[1] *Key Laboratory of Mesoscopic Chemistry of MOE and Collaborative Innovation Center of Chemistry for Life Sciences, School of Chemistry and Chemical Engineering, Nanjing University, Nanjing 210093, China*
[2] *Department of Chemistry, Duke University, Durham, NC 27708, USA*

Received: 13 November 2016
Revised: 10 February 2017
Accepted: 11 February 2017

KEYWORDS
tin disulfide,
metal dichalcogenides,
two-dimensional materials,
atomic steps,
photoconductivity and light-sensing

ABSTRACT

We demonstrated the controlled growth of two-dimensional (2D) hexagonal tin disulfide (SnS_2) nanoflakes with stacked monolayer atomic steps. The morphology was similar to flat-topped and step-sided mesa plateaus or step pyramids. The SnS_2 nanoflakes were grown on mica substrates via an atmospheric-pressure chemical vapor deposition process using tin monosulfide and sulfur powder as precursors. Atomic force microscopy (AFM), electron microscopy, and Raman characterizations were performed to investigate the structural features, and a sequential layer-wise epitaxial growth mechanism was revealed. In addition, systematic Raman characterizations were performed on individual SnS_2 nanoflakes with a wide range of thicknesses (1–100 nm), indicating that the A_{1g} peak intensity and Raman shifts were closely related to the thickness of the SnS_2 nanoflakes. Moreover, photoconductive AFM was performed on the monolayer-stepped SnS_2 nanoflakes, revealing that the flat surface and the edges of the SnS_2 atomic steps had different electrical conductive properties and photoconductive behaviors. This is ascribed to the dangling bonds and defects at the atomic step edges, which caused a height difference of the Schottky barriers formed at the interfaces between the PtIr-coated AFM tip and the step edges or the flat surface of the SnS_2 nanoflakes. The 2D SnS_2 crystals with regular monolayer atomic steps and fast photoresponsivity are promising for novel applications in photodetectors and integrated optoelectronic circuits.

1 Introduction

In recent years, two-dimensional (2D) atomic crystals, especially graphene, have been extensively studied owing to their fascinating electrical, mechanical, and optical properties [1–7]. However, the narrow bandgap

Address correspondence to Zhong Jin, zhongjin@nju.edu.cn; Jie Liu, j.liu@duke.edu

of graphene limits its potential applications in electronic devices; hence, it is of great importance to explore other 2D-layered materials [8, 9]. Among these, layered metal chalcogenides, including transition-metal chalcogenides (such as MoS_2 [10–16], $MoSe_2$ [17, 18], and WS_2 [19, 20]) and main-group metal chalcogenides (such as GaS [21, 22], In_2S_3 [23], In_2Se_3 [24], $SnSe_2$ [25], Sb_2S_3 [26], and Bi_2Se_3 [27, 28]), have emerged as a new class of 2D nanomaterials with a highly adjustable band structure and great potential for diverse applications in nanoelectronics and photodetectors. However, the structural control of 2D metal chalcogenide crystals, such as the precise adjustment of the thickness, morphology, and grain boundaries and the formation of layered atomic steps, remains a challenging problem.

Among semiconductive metal dichalcogenides, tin disulfide (SnS_2) is a promising candidate for field-effect transistors and photodetectors because of its appropriate indirect bandgap (2.03 eV in monolayer material and 2.31 eV in bulk material), high carrier mobility (up to 230 $cm^2 \cdot V^{-1} \cdot s^{-1}$), large on–off ratio (>$10^6$), and high photoresponsivity (100 $A \cdot W^{-1}$) [29–33]. Recently, mechanical and chemical exfoliation have been performed to isolate few-layered SnS_2 nanoflakes from bulk crystals for photocatalytic water splitting and field-effect transistors [30–32]. Another effective method for synthesizing single-crystal SnS_2 nanoflakes is chemical vapor deposition (CVD). Peng et al. reported the CVD growth of SnS_2 crystal arrays at predefined seeding locations on SiO_2 substrates for fast photodetectors [29]. Meng et al. developed a CVD process for the screw-dislocation-driven spiral growth of SnS_2 nanoflakes several hundred nanometers thick [33]. However, most of the SnS_2 nanoflakes reported in the literature have a large thickness (dozens of nanometers to hundreds of nanometers) and no stacked monolayer atomic step structures [33–35]. Moreover, the detailed growth mechanism and thickness-dependent photoelectronic properties of ultrathin SnS_2 materials must be explored.

In this study, we grew ultrathin hexagonal SnS_2 nanoflakes via an atmospheric-pressure CVD (APCVD) method using stannous sulfide (SnS) and sulfur as novel precursor materials. By controlling the reaction conditions, the precise growth of monolayer atomic steps on hexagonal nanoflakes with a similar shape to mesa plateaus or step pyramids was achieved. In addition, we proposed the sequential layer-wise growth mechanism of mesa-shaped SnS_2 nanoflakes initiated from monolayer SnS_2 seeds. This mechanism is distinct from those previously reported, such as the screw-dislocation mechanism [33]. According to the proposed mechanism, the thickness of the SnS_2 nanoflakes can be well-controlled from the monolayer thickness to ~100 nm. Microscopic Raman analysis was performed to investigate the thickness-dependent evolution of the peak intensities and band positions. Moreover, the photoresponsive properties of the mesa-shaped SnS_2 nanoflakes were investigated, revealing thickness-dependent photoconductivity, as well as different photoresponse behaviors between the step edges and the flat surface of the SnS_2 nanoflakes.

2 Experimental

2.1 APCVD growth of mesa-like SnS_2 nanoflakes

The growth was performed using a tube furnace with a 1-in inner diameter and a 28-cm-long heating zone. First, a quartz boat containing 20 mg of SnS power (Aladdin) was placed at the center of the heating zone, and another quartz boat containing 150 mg of sulfur power (Aladdin) was placed 15 cm upstream from the SnS precursor. Freshly exfoliated mica substrates were placed 12 cm downstream from the SnS precursor. A gas flow of 50 sccm Ar was introduced to remove the residual air. The tube furnace was gradually heated to 550 ℃ within 20 min and maintained at this temperature for 15 min to grow the SnS_2 nanoflakes. In this process, the temperatures of the sulfur precursor and mica substrates were maintained at approximately 200 and 450 ℃, respectively. After the growth, the tube furnace was cooled naturally to room temperature. To investigate the growth mechanism of the SnS_2 nanoflakes with the monolayer atomic steps, different growth times (1, 5, and 30 min) were used in control experiments.

2.2 Transfer of SnS_2 nanoflakes from mica to other substrates

The SnS_2 nanoflakes were transferred to transmission

electron microscopy (TEM) grids or indium tin oxide (ITO) glass with the assistance of poly(methyl methacrylate) (PMMA). First, a PMMA solution (4 wt.% in anisole) was spin-coated onto the mica substrate with SnS_2 nanoflakes at a speed of 2,500 rpm for 1 min, followed by annealing at 120 ℃ for 5 min. Then, the substrate was immersed in an HF solution (5 wt.%). After 30 min, the PMMA film with attached SnS_2 nanoflakes was separated from the mica and suspended on the surface of the HF solution. Then, the PMMA film was transferred to the surface of deionized water and fished out using TEM grids or ITO glass. After naturally drying in air at room temperature, the PMMA film was dissolved by warm acetone (50 ℃) and dried by a N_2 flow.

2.3 Structural characterizations of SnS_2 nanoflakes

Optical images and Raman spectra were collected using a confocal Raman spectroscope (Horiba, LabRAM Evolution) with a 473-nm laser, a 50× objective lens, a spot size ~3 μm in diameter, and a grating of 1,800 lines·mm^{-1}. All of the Raman spectra were collected with an exposure time of 3 s and accumulated 10 times. TEM was performed using a JEM-2100 system with an operation voltage of 200 kV.

2.4 Photoconductive atomic force microscopy (AFM) measurements of SnS_2 nanoflakes on ITO

Topographic and photoconductive AFM characterizations were performed using a Bruker Dimension Icon instrument. The ScanAsyst model and ScanAsyst-Air probes were used to measure the morphology and thickness of the nanoflakes. The Peakforce-Tune model and SCM-pic IrPt conductive probes were used to measure the adhesion force mapping and photoresponse properties. A laser diode (LSFLD405-3, Beijing LST Ltd.) with a spot area of 0.25 mm^2 and a light power density of 1,200 mW·cm^{-2} was used as the light source, with an operation voltage and working current of 4.8 V and 35 mA, respectively. The laser was used to illuminate designated SnS_2 nanoflakes on the ITO substrate via a single mode optical fiber and an optical fiber splice (FC-PC) connecting the optical fiber and the laser diode. Ramp mode and strip chart controls were used to acquire the current–voltage (*I*–*V*) and current–time curves, respectively. All the operational parameters were fixed for current mapping in the dark and under illumination.

3 Results and discussion

As shown in Fig. 1(a), hexagonal SnS_2 nanoflakes were grown on mica via APCVD at 550 ℃ by using SnS and sulfur as precursors (additional details are provided in the Experimental section). To our knowledge, the synthesis of SnS_2 nanoflakes with SnS and sulfur as precursors has not been reported. Compared with the common strategies using SnO_2 as the precursor [29, 34, 36–39], the newly adopted tin source (SnS) is advantageous for the crystallization of SnS_2 nanoflakes because the energy of the Sn–S bond (464 kJ·mol^{-1}) is lower than that of the Sn–O bond (532 kJ·mol^{-1}) [35] and the absence of oxygen is favorable for the growth of high-crystallinity SnS_2 crystals without oxygen defects. Moreover, the growth conditions used in this study (550 ℃, atmospheric pressure) are considerably milder than those of previous reports (700 ℃, low pressure) [29, 34]. Mica was selected as the substrate owing to its chemical inertness, atomically smooth surface without dangling bonds, and high flexibility for the fabrication of bendable devices [40].

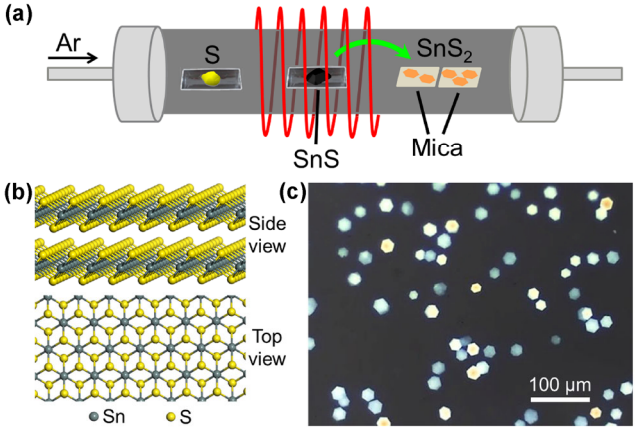

Figure 1 Synthesis and optical characterizations of the hexagonal SnS_2 nanoflakes with atomic steps. (a) Schematic illustration of the APCVD process for the synthesis of the SnS_2 nanoflakes. SnS and sulfur were used as the tin and sulfur sources, respectively. Mica sheets were placed downstream as receiving substrates. (b) Side and top views of the layered SnS_2 atomic structure. (c) Optical microscopy image of the as-grown hexagonal SnS_2 nanoflakes on mica, showing large-area hexagonal SnS_2 nanoflakes between 8 and 17 μm in length.

Figure 1(b) shows top and side views of the layered SnS_2 atomic structure, which had a CdI_2-type crystal structure with octahedral metal coordination [41]. Each SnS_2 monolayer was formed by covalently bonded tin and sulfur atoms, and the neighboring layers interacted via a weak van der Waals force. The monolayer SnS_2 nanoflakes on the mica substrate were almost invisible under the optical microscope owing to the low contrast, but few-layer SnS_2 nanoflakes were clearly observed. Figure 1(c) shows a typical large-area optical image of the as-prepared hexagonal SnS_2 nanoflakes, indicating lengths in the rage of 8–17 μm. The color of the nanoflakes observed using the optical microscope was closely related to the thickness. In general, the SnS_2 nanoflakes with a darker color (blue) were thinner, and those with a brighter color (white) were thicker. Moreover, the white edges (thinner part) and light yellow centers (thicker part) of the SnS_2 nanoflakes indicate a thickness gradient, which originated from the atomic steps. To investigate the color evolution corresponding to the thickness variation of the SnS_2 nanoflakes, optical images of nanoflakes with different thicknesses were examined, as shown in Fig. S1(c) (in the Electronic Supplementary Material (ESM)). The color change of the nanoflakes can be divided into two stages corresponding to the thickness ranges of 3–30 and 30–90 nm. Because the nanoflakes were thinner than 10 nm at the first stage, most of the light penetrated through the nanoflakes, and only small part of the light was reflected. The color of the nanoflakes changed from light blue to bright white as the thickness increased from 3 to 30 nm, indicating the enhanced reflection light intensity. However, when the thickness further increased from 30 to 90 nm at the second stage, the color of the nanoflakes changed from light yellow to deep yellow owing to the enhanced optical absorption of the SnS_2 crystals under visible-light with different wavelengths and the optical interference of light reflected from the bottom and top surfaces. Additional optical images are provided in Figs. S1(a) and S1(b) (in the ESM), indicating the uniform distribution of the SnS_2 nanoflakes over the entire substrate. The large amount of SnS_2 nanoflakes grown on the mica substrate allowed the direct characterization of the crystalline structure via X-ray diffraction (XRD) analysis, as shown in Fig. S2 (in the ESM). To distinguish the weak peaks of SnS_2 from the strong peaks of mica, the area indicated by the red rectangle in Fig. S2(a) (in the ESM) was magnified, as shown in Fig. S2(b) (in the ESM), confirming that the as-synthesized nanoflakes were 2T-phase SnS_2 (JCPDS PDF card No. 23-0677). The calculated lattice constants (a = b = 0.3632 nm and c = 0.588 nm) of the SnS_2 nanoflakes are comparable to the theoretical values (a = b = 0.3645 nm, c = 0.589 nm) [42], indicating the high crystallinity. For 2T-phase layered metal dichalcogenides, the letter "T" represents "trigonal," and the digit "2" indicates the number of layers in the stacking sequence [43, 44]. The stacking sequence of the as-synthesized SnS_2 nanoflakes was AbC CaB.

The morphology of a typical hexagonal SnS_2 nanoflake was investigated via AFM, as shown in Fig. 2(a). The width of the hexagon was ~12 μm, and the central thickness was ~12 nm. A mesa-like structure was clearly observed (Fig. 2(a)), and the length of each SnS_2 layer gradually decreased from the bottom to the top. Figure 2(b) presents a magnified AFM image of the area indicated by the red square in Fig. 2(a), showing clearly hexagonal atomic steps. Figure 2(c) shows the height profile corresponding to the blue line in Fig. 2(b). The height of each atomic step was ~0.59 nm, corresponding to a single layer of SnS_2. The height of the atomic steps is consistent with the interplanar spacing of the bulk SnS_2 crystal (~0.589 nm) and the XRD analysis results, indicating the epitaxial growth of high-quality SnS_2 nanoflakes. Similar step structures are observed for other metal sulfides [45–48] but with significantly fewer monolayers than the mesa-shaped SnS_2 nanoflakes obtained in this study. The preferential planar growth is attributed to the high-energy edges and dangling bonds located at the sides of the atomic steps, which bonded with intermediate species far more easily than the flat surface. Each layer of the mesa-like nanoflake was hexagonal (Fig. 2(b)); however, a roughly trigonal shape was observed in some cases, owing to the different atomic diffusion rates along the a and b directions of the crystalline domain [49]. Figures S3(a) and S3(b) (in the ESM) show a case where all the stacked layers were hexagonal SnS_2 monolayers. Occasionally, several nucleus/seeds were very close and interacted to form a single nanoflake; thus, several separated upper

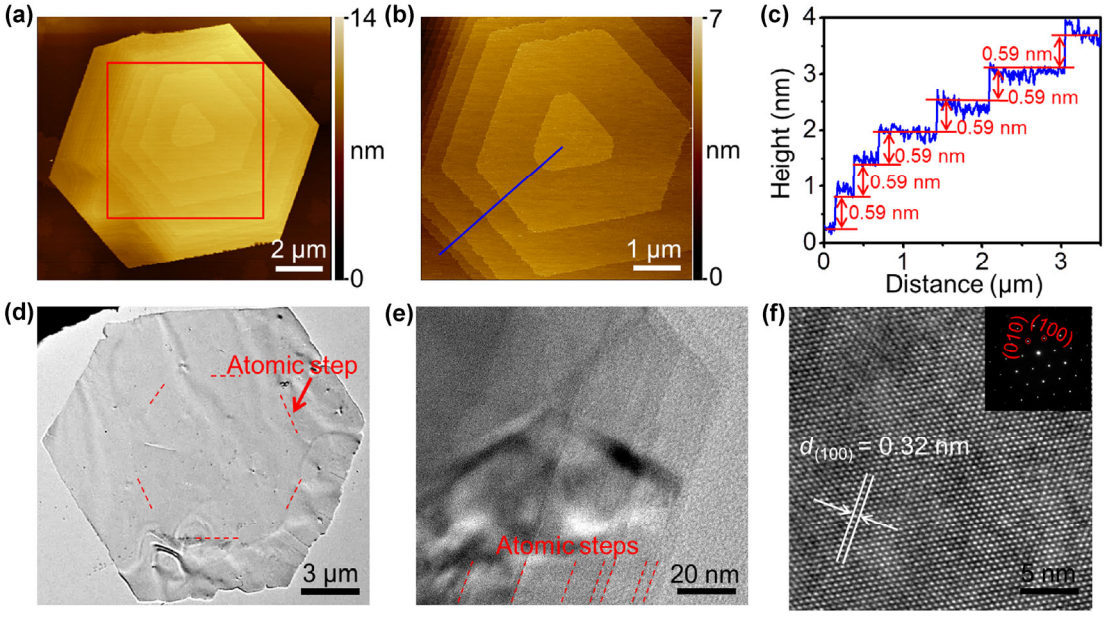

Figure 2 AFM and TEM characterizations of the mesa-shaped SnS_2 nanoflakes with monolayer atomic steps. (a) AFM image of an as-prepared SnS_2 nanoflake ~12 μm in width. (b) AFM image measured for the area indicated by the red framework in (a), clearly showing the hexagonal shape of the stacked atomic steps. (c) Height profile extracted from the blue line in (b). The height of each atomic step was measured to be ~0.59 nm. (d) TEM image of a typical hexagonal SnS_2 nanoflake with a thickness gradient. The boundary of one atomic step is highlighted by red dashed lines. (e) TEM image of the edge of the hexagonal SnS_2 nanoflake, in which the atomic steps (marked by red dashed lines) are clearly observed. (f) High-resolution TEM image of the nanoflake in (d), showing a lattice spacing of 0.32 nm, which is identical to that of the (100) planes of SnS_2. The inset shows a SAED pattern, demonstrating a single-crystalline hexagonal phase.

planes were observed at the top of the bottom plane (Figs. S3(c) and S3(d) in the ESM).

To investigate the crystal structure, the SnS_2 nanoflakes were characterized via TEM. Figure 2(d) shows a TEM image of a typical hexagonal SnS_2 nanoflake ~9 μm in width. Its stepped structure is highlighted by the red dashed lines in the figure. Atomic steps were clearly observed at the edge of the hexagonal nanoflakes (Fig. 2(e) and Fig. S4(a) in the ESM, as marked by red dashed lines). High-resolution TEM images (Fig. 2(f) and Fig. S4(b) in the ESM) show ordered lattice fringes with a spacing of 0.32 nm, corresponding to the (100) planes of the SnS_2 crystal. The hexagonal symmetrical selected-area electron diffraction (SAED) pattern shown in the inset of Fig. 2(f) confirms the single-crystalline feature of the as-obtained SnS_2 nanoflakes.

To further investigate the growth mechanism of the mesa-shaped SnS_2 nanoflakes, control experiments with different growth times were performed. AFM images of samples grown for 1, 5, 15, and 30 min are shown in Figs. 3(a)–3(d), respectively, and the corresponding height profiles for the blue lines in the AFM images are also provided. Initially, when the growth time was 1 min, tiny SnS_2 seeds with relatively irregular shapes, an average diameter of ~500 nm, and a very uniform thickness of ~1.0 nm were randomly formed on the mica substrate (Fig. 3(a)). Notably, all of the SnS_2 seeds occurred as a monolayer. The height of the monolayer SnS_2 seeds measured by AFM (~1.0 nm) was larger than the intrinsic interlayer spacing of SnS_2, which is attributed to the tip–sample and sample–substrate interactions [50]. On the other hand, the mismatch between the lattice constants of mica [51] (0.531 nm) and SnS_2 [33] (0.365 nm) may have caused the irregular shape of the SnS_2 seeds. When the growth time was increased to 5 min, regular hexagonal SnS_2 nanoflakes with the thickness of several nanometers were formed, as shown in Fig. 3(b). A newly grown SnS_2 layer with an atomic step height of ~0.59 nm was observed on top of the original nanoflakes. When the reaction time was increased to 15 min, the hexagonal

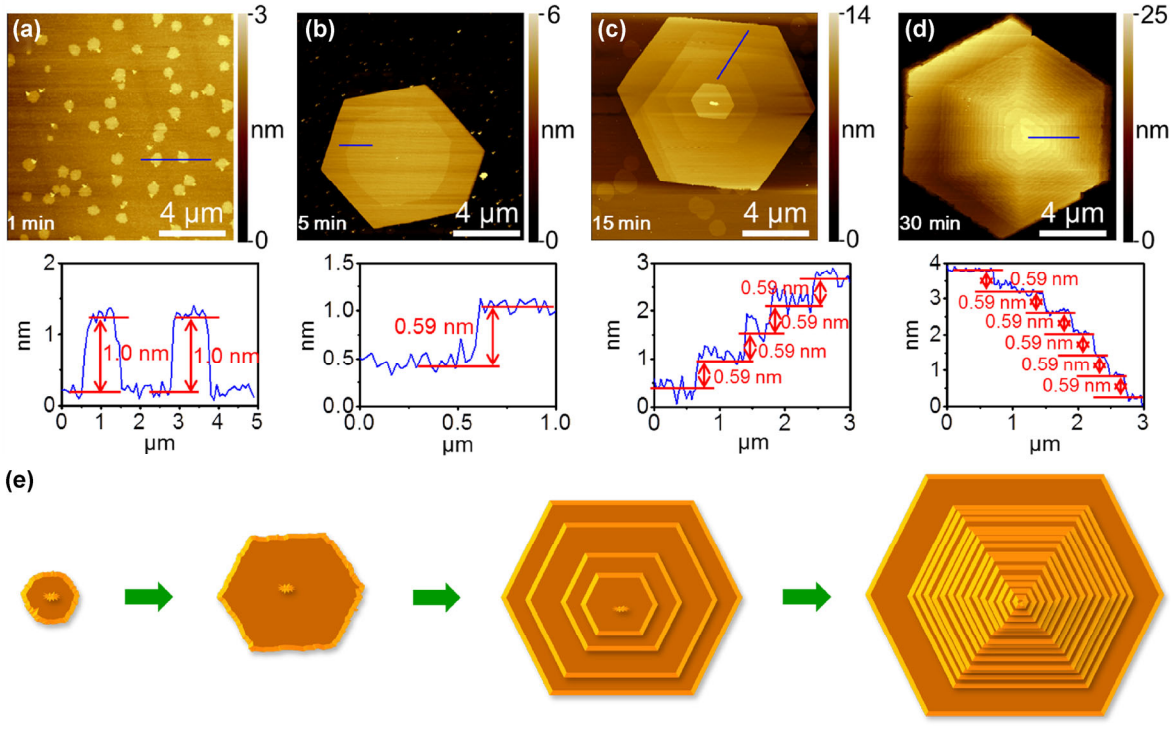

Figure 3 (a)–(d) AFM characterizations (top) and corresponding height profiles (bottom, collected from the blue lines in the above AFM images) for the SnS_2 nanoflakes at different growth stages. (e) Schematic illustration of the proposed layer-wise epitaxial growth mechanism for the mesa-shaped SnS_2 nanoflakes at different growth stages.

SnS_2 nanoflakes became larger and thicker, and the entire morphology gradually transformed into mesa plateaus with a flat top and stacked monolayer atomic steps (Fig. 3(c)). Notably, the newly formed upper layers maintained a relatively regular hexagonal shape and the same orientation as the bottom layer. Eventually, the layered nanoflakes exhibited a morphology similar to step pyramids, with numerous monolayer atomic steps and a thickness of dozens of nanometers at the center (Fig. 3(d)). The morphological evolution of the stacked hexagonal SnS_2 nanoflakes indicates a sequential layer-wise growth mechanism (Fig. 3(e)). We propose that the 2D SnS_2 nanoflakes were grown via an epitaxial growth process with layer-wise growth stages, which differs from the growth of other metal chalcogenides [52–56]. First, the bottom layer of the SnS_2 nanoflake was formed around an initial seed, which functioned as the crystallization nucleus. This is frequently observed at the center of the SnS_2 nanoflakes in the AFM images (Figs. 3(b) and 3(c)). We measured the length difference between the bottom and top layers of the mesa-shaped SnS_2 nanoflakes and found that the top layer began to grow when the length of the bottom layer was approximately 1.2–2.3 μm. As the reaction time increased, the nanoflakes became larger and exhibited a more regular hexagonal shape, owing to the epitaxial growth along the lateral *a* and *b* directions. Then, new layers were grown on the bottom layer, forming monolayer atomic steps, as shown in Fig. 3(e). Owing to the sequential growth of the different layers and the inconsistent diffusion rate at the edges, the growth time and growth rate differed among the layers. Therefore, the lateral sizes of the hexagonal monolayers from the bottom to the top were arranged from large to small. Because of the favorable lattice matching between the newly deposited layer and the existing layers, the stacked atomic steps preferred to share an identical lattice orientation. Thus, the stacked hexagonal SnS_2 nanoflakes with the shape of mesa plateaus or step pyramids were formed.

Raman spectroscopy is a simple and accurate method for determining the thickness of 2D metal chalcogenides, as the Raman signals of 2D atomic

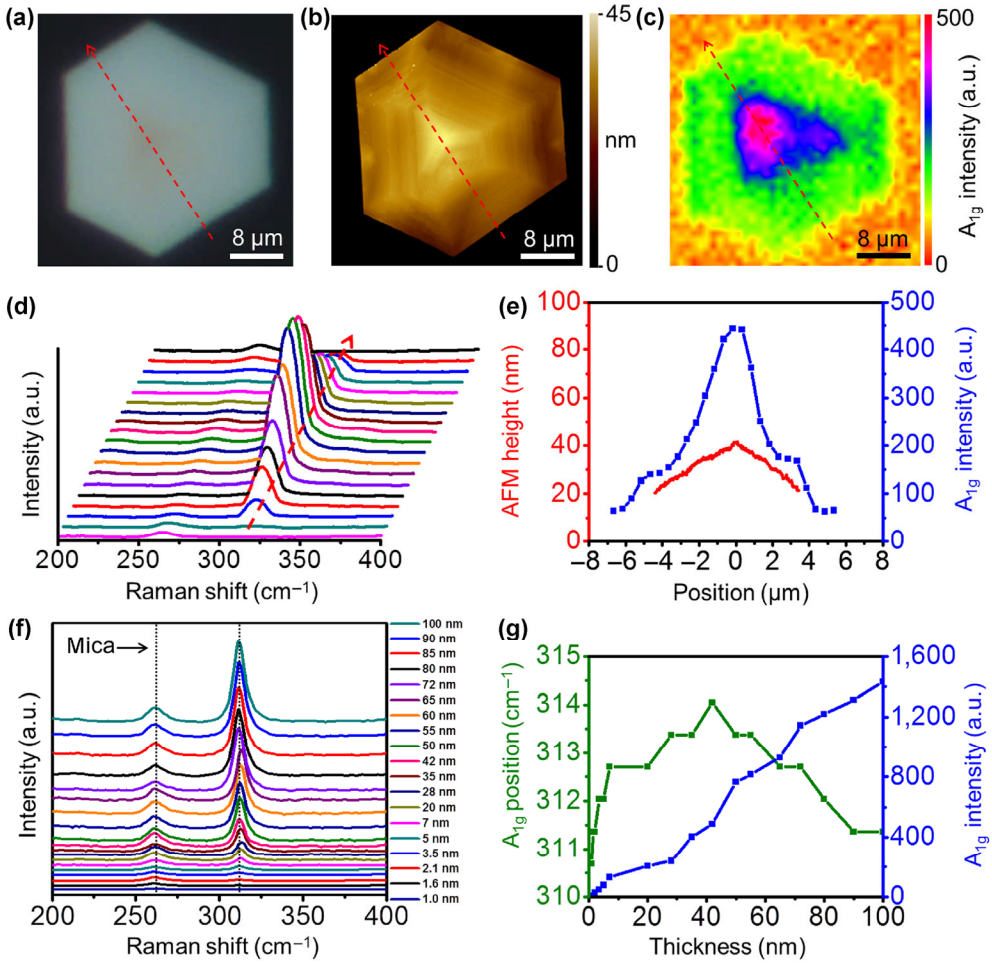

Figure 4 *In situ* Raman characterizations of the mesa-shaped SnS_2 nanoflakes. (a) Optical image and (b) corresponding AFM image of a mesa-shaped SnS_2 nanoflake. (c) Raman scanning of the same mesa-shaped SnS_2 nanoflake, showing the 2D mapping of the A_{1g} peak intensity. The excitation laser wavelength was 532 nm. (d) Independent Raman spectra measured along the red dashed lines in (a)–(c). (e) AFM height profile (red line) and A_{1g} peak-intensity profile (blue line) measured along the red dashed lines in (a)–(c). The variation of the A_{1g} peak intensity is consistent with the thickness gradient of the SnS_2 nanoflake. (f) Raman spectra for the center of the SnS_2 nanoflakes with different thicknesses, showing that the intensity and position of the A_{1g} peak varied with respect to the thickness. (g) A_{1g} peak positions (green line) and A_{1g} peak intensities (blue line) calculated for the Raman spectra in (f) with respect to the thickness.

crystals typically vary according to the layer number. For example, the E^1_{2g} and A^1_g band positions of MoS_2 change monotonously with respect to the layer number [57]. To our knowledge, only one article has reported the evolution of the Raman intensity with respect to the layer number of mechanically exfoliated SnS_2 crystals [30]. However, the thickness of the SnS_2 characterized in that study ranged from 1 to 10 nm, and the thickness-dependent Raman peak shifts of SnS_2 have not been investigated. In the present study, for the first time, we systematically analyzed the thickness-dependent Raman-signal evolution for CVD-grown SnS_2 nanoflakes. For a control sample of bulk SnS_2 crystal with a thickness of >120 nm, a strong peak at 314.1 cm^{-1} and a weak peak at 204.9 cm^{-1} were observed, which are assigned to the characteristic A_{1g} and E_g modes, respectively (Fig. S5(a) in the ESM). The mode of E_g at 204.9 cm^{-1} indicates that the SnS_2 crystal had a 2T phase [29, 30, 43]. As the layer number of the SnS_2 nanoflakes decreased below 120 nm, the in-plane scattering was reduced, causing the disappearance of E_g mode and the intensity reduction of the A_{1g} mode [29]. To identify the position and intensity variation of the A_{1g} mode in the SnS_2

nanoflakes with a thickness gradient and atomic steps (as shown in Figs. 4(a) and 4(b)), we performed *in situ* large-area 2D Raman mapping. Figure 4(c) shows the A_{1g} peak-intensity mapping of a SnS_2 nanoflake. As indicated by the distinct color contrast, the thickness and the A_{1g} peak intensity were closely related. The top platform of the mesa-shaped SnS_2 nanoflake with maximum height exhibited the highest intensity of the A_{1g} mode, as indicated by the red color in Fig. 4(c). The Raman spectra collected along the red dashed lines in Figs. 4(a)–4(c) are shown in Fig. 4(d), demonstrating that the variation of the A_{1g} peak intensity strongly depended on the thickness. Figure 4(e) shows the height profile measured via AFM (red line) and the A_{1g} peak-intensity profile (blue line) collected along the red dashed lines in Figs. 4(a)–4(c). The trends of these two profiles match very well.

The Raman-signal evolution of SnS_2 nanoflakes with different thicknesses was also investigated, as shown in Fig. 4(f). The peak around 264.5 cm^{-1} originated from the mica substrate. Clearly, both the intensity and position of the A_{1g} peak strongly depended on the thickness of the SnS_2 nanoflakes. The intensity profile (blue line) and position profile (green line) of the A_{1g} peak with respect to the thickness are shown in Fig. 4(g). In the thickness range of 1–100 nm, the A_{1g} peak intensity increased almost monotonically with increasing thickness. Similarly, the peak area of the A_{1g} mode exhibited a linear relationship with the thickness (Fig. S5(b) in the ESM). However, the position of the A_{1g} peak exhibited a volcano-type dependence, as depicted by the green line in Fig. 4(g). As the thickness increased from 1.0 to 42 nm, the wavenumber of the A_{1g} peak increased from 310.7 to 314.1 cm^{-1}. However, when the thickness of the SnS_2 nanoflakes increased from 42 to 100 nm, the wavenumber of the A_{1g} peak decreased from 314.1 to 311.4 cm^{-1}. When the thickness increased, the increased interlayer van der Waals force in the SnS_2 nanoflakes suppressed the atomic vibration, yielding higher force constants [57]. However, the long-range interlayer Coulomb repulsion derived from the electron pairs of the bonding atoms exhibited the opposite effect [58]. The A_{1g} peak blue-shifted when the thickness of the SnS_2 nanoflakes increased from 1 to 42 nm, which is attributed to the increased force constant resulting from the enhanced interlayer van der Waals force [57]. In contrast, the A_{1g} peak redshifted when the thickness of the SnS_2 nanoflakes increased from 42 to 100 nm, suggesting that the long-range interlayer Coulomb repulsion dominated the change in the atomic vibration, while the increased interlayer van der Waals force played a secondary role [57–61]. Unlike the A_{1g} peak intensity, area, and position, the full width at half maximum decreased rapidly from 11.0 to 7.3 cm^{-1} when the thickness increased from 1.0 to 7.0 nm and then remained relatively constant (~7.5 cm^{-1}) with the further increase of the thickness (Fig. S5(c) in the ESM). These results indicate that Raman spectroscopy was effective for identifying the crystal thickness of the CVD-grown SnS_2 nanoflakes.

The photoconductive properties of the SnS_2 nanoflakes were investigated via photoconductive AFM, as illustrated in Fig. 5(a). The SnS_2 nanoflakes were transferred onto ITO conductive glass with the assistance of PMMA. The ITO substrate used in this study was heavily n-doped and had a work function (Φ_{ITO}) of ~4.7 eV, a bandgap of 3.5 eV [62, 63], and an electron affinity of ~4.1 eV [64]. The ITO glass was placed on the chunk of AFM, and a cable was used to connect the ITO substrate to the cantilever mounted with the conductive AFM tip. Similar to previous studies [65, 66], standard Ptlr conductive tips were used to perform photoconductive AFM experiments on the SnS_2 nanoflakes. By applying a voltage to the ITO substrate, current signals were detected using a digital ammeter. Figure 5(b) and Fig. S6(a) in the ESM show the AFM adhesion force mapping and a corresponding topographic AFM image of a mesa-shaped SnS_2 nanoflake with a maximum thickness of 75 nm. The monolayer atomic steps on the nanoflake are clearly observed in Fig. 5(b); however, they cannot be clearly observed in Fig. S6(a) (in the ESM), owing to the large height scale. The photoconductive AFM images of the mesa-shaped SnS_2 nanoflakes in the dark and under light illumination are illustrated in Figs. 5(c) and 5(d), respectively. Interestingly, the step edges and the flat surfaces of the SnS_2 atomic steps exhibited very different conductivity in the dark; thus, they were easily distinguished (Fig. 5(c)). The conductivity at the edges of the atomic steps was obviously higher than that on the flat surfaces. Under

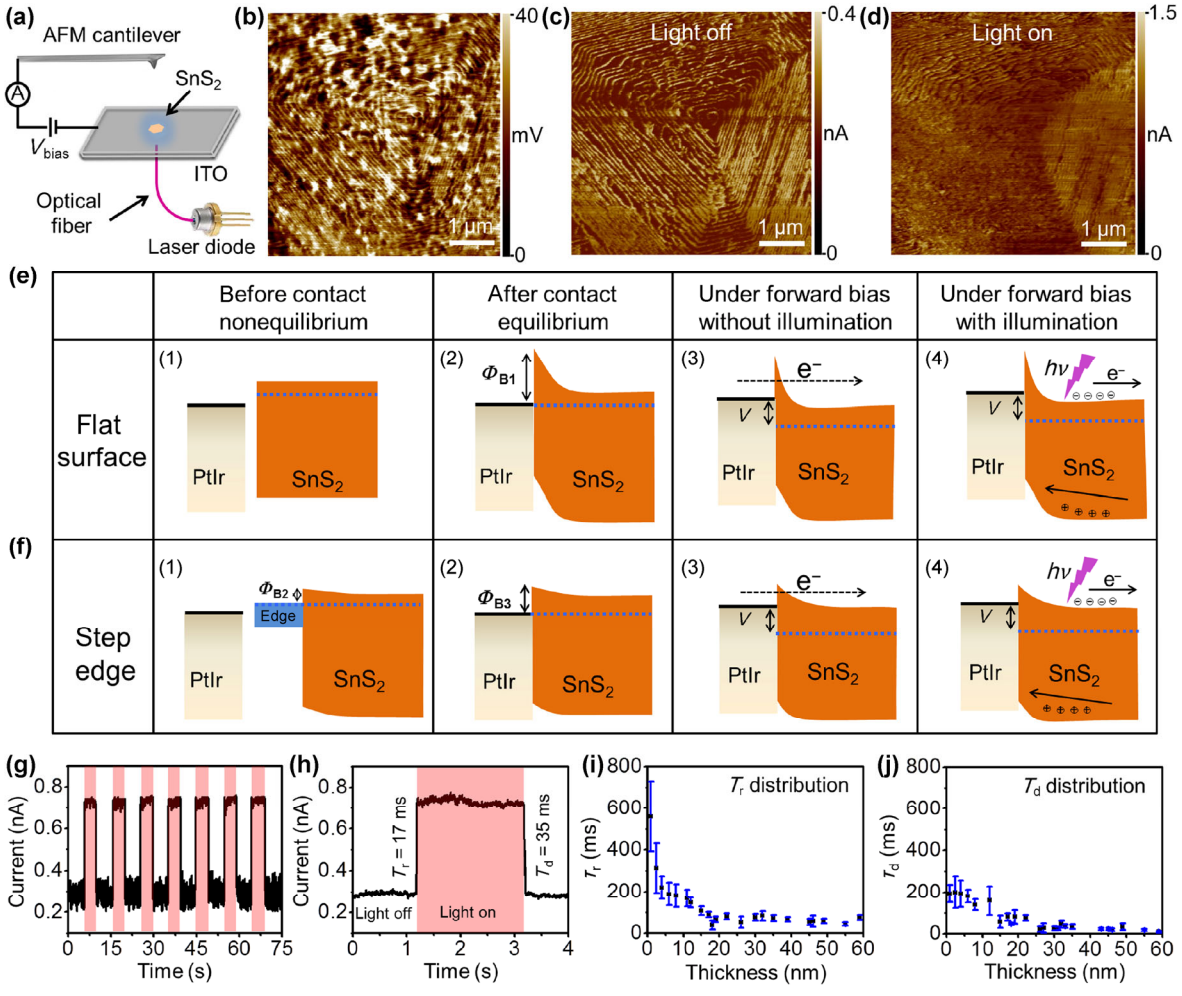

Figure 5 Photoconductive AFM characterizations of the mesa-shaped SnS_2 nanoflakes. (a) Photoconductive AFM apparatus setup. (b) AFM adhesion-force mapping of a mesa-shaped SnS_2 nanoflake. (c) Corresponding conductive AFM image measured in the dark at a bias of 1.0 V. (d) Corresponding photoconductive AFM image of the SnS_2 nanoflake in (b) and (c) measured under light illumination at a wavelength of 405 nm. (e) and (f) Schematic interfacial band diagrams of a PtIr metal-coated AFM tip–mesa-shaped SnS_2 nanoflake flat surface junction (tip–surface junction) and PtIr metal-coated AFM tip–mesa-shaped SnS_2 nanoflake step edge junction (tip–edge junction), respectively. The diagrams show the interfacial band structure of the tip–surface and tip–edge junctions (1) before contact, (2) after contact, (3) under forward bias without illumination, and (4) under forward bias with illumination. (g) Time-resolved photoresponse measured for the top layer of a SnS_2 nanoflake with a thickness of 18 nm. The periods of light illumination are highlighted in a light red color. (h) Photocurrent rise and decay curves for the same nanoflake in (g), indicating a T_r of ~17 ms and a T_d of ~35 ms. (i) and (j) Statistical analysis of T_r and T_d, respectively, with respect to the thickness of the SnS_2 nanoflakes.

405-nm light illumination generated by a monocolor laser diode, a strong photoresponse was detected via photoconductive AFM (as shown in Fig. 5(d)). The conductivity difference between the step edges and the flat surfaces of the atomic steps was significantly reduced under the illumination (Fig. 5(d)), confirming that the current intensity depended on the surface properties and local photoresponse properties rather than on the topography.

To evaluate the possible photoinduced thermoelectric effect on the SnS_2 nanoflakes, the following theoretical model was used for estimating the vertical temperature profile of the SnS_2 nanoflakes [67]

$$T(x) = \frac{Qx}{\kappa A} + T_0 \quad (1)$$

Here, Q is the absorbed laser power, x is the distance from the top surface (maximum value at the bottom

surface of the SnS_2 nanoflake and zero at the top surface of the nanoflake), A is the cross-sectional area, T_0 is room temperature, and κ is the thermal conductivity. The thermoelectric voltage generated by the photoinduced thermoelectric effect was calculated using the following equation [67]

$$V = \int_0^h S \frac{\mathrm{d}T}{\mathrm{d}x} \mathrm{d}x \quad (2)$$

Here, S is the Seebeck coefficient. In this study, Q was ≤1.2×10^{-6} W (assuming that most or all of the laser power was absorbed by the SnS_2 nanoflake), and A was estimated to be ~100 μm^2. According to a previous report regarding the thermoelectric effect of SnS_2 crystals [68], the S and κ of SnS_2 were estimated to be 34.7 mV·K^{-1} and ~3.45 W·m^{-1}·K^{-1}, respectively. Therefore, the photoinduced thermoelectric voltage of the SnS_2 nanoflakes was estimated to be $V \leq 1.0 \times 10^{-9} h$ V·nm^{-1}. For a typical SnS_2 nanoflake with a thickness of 16 nm, the thermoelectric voltage between the bottom and top surfaces was ≤1.6×10^{-8} V, which is far lower than the bias applied to the ITO electrode (1.0 V). Thus, the photoinduced thermoelectric effect can be ignored in our study.

The photoresponse behavior indicates the formation of different energy barriers between the PtIr metal-coated AFM tip and the SnS_2 flat surface and between the PtIr metal-coated AFM tip and the SnS_2 atomic step edge both with and without illumination. The corresponding band-structure diagrams are shown in Figs. 5(e) and 5(f), respectively. According to the Schottky–Mott theory [69], the difference between the work function of the PtIr-coated AFM tip (Φ_{PtIr} = 5.4 eV [70]) and the conduction-band minimum (CBM) of the inert SnS_2 flat surface (E_{CBM} = −4.4 eV [71]) could have yielded a Schottky barrier Φ_{B1} at the tip–surface junction. The height of the Schottky barrier was estimated to be 1.0 eV (Fig. 5(e)(2)). For the step edges, the unpaired electrons in the dangling bonds and the edge defects formed an electronic edge state with a relatively narrow energy band, and an energy barrier Φ_{B2} was formed between the bulk n-type SnS_2 crystal and the step edges (Fig. 5(f)(1)) [72, 73]. When the PtIr-coated AFM tip was in contact with the SnS_2 step edges, the edges partially decreased the work-function difference between the AFM tip and the SnS_2 crystal; thus, the tip–edge interface energy barrier Φ_{B3} (Fig. 5(f)(2)) was smaller than the tip–surface interface energy barrier Φ_{B1} (Fig. 5(e)(2)) [74, 75]. Under a forward bias and without illumination (Figs. 5(e)(3) and 5(f)(3)), the barrier height and the direction of the charge injection limited the thermionic emission to the lowest saturation, resulting in an enhanced probability of field-emission tunneling through the energy barrier [65, 66]. Therefore, the barrier-height difference made the current flowing through the tip–surface junction (Fig. 5(e)(3)) smaller than that flowing through the tip–edge junction (Fig. 5(f)(3)). Under a forward bias with light illumination, photogenerated electrons accumulated at the ITO substrate because no appreciable barrier difference formed at the SnS_2–ITO junction, decreasing the difference between the currents flowing through the tip–surface junction (Fig. 5(e)(4)) and the tip–edge junction (Fig. 5(f)(4)) [65]. The corresponding I–V plots (Fig. S6(b) in the ESM) were measured at the top platform of this SnS_2 nanoflake (ramped at the red point in Fig. S6(a) in the ESM) in the dark (black line) and under illumination (red line), revealing that the conductivity of the SnS_2 nanoflake under illumination was significantly higher than that in the dark. This result is consistent with the photo-conductive AFM mapping (Figs. 5(c) and 5(d)).

The time-resolved photoconductive characteristics were investigated by periodically turning a light on and off. The photoresponse curve measured for the top platform of a mesa-shaped SnS_2 nanoflake with a thickness of 18 nm is shown in Figs. 5(g) and 5(h), showing the quantitatively acquired photoresponse times. The photocurrent rise time (T_r) and decay time (T_d) of the SnS_2 nanoflake were measured as ~17 and ~35 ms, respectively (Fig. 5(h)), indicating a fast response to light. The contact properties may have depended on the surface states where the AFM tip was located or on the force applied to the tip. Therefore, we measured the photoresponse time of another SnS_2 nanoflake with a thickness of 30 nm at different positions with the same applied force on the AFM tip (Fig. S7(a) in the ESM) and at the same position with different applied forces (Fig. S7(b) in the ESM). As shown in Fig. S7 (in the ESM), the tip location and contact force/pressure had a very small influence on the photoresponse time. This confirms that the fast

and notable photoresponse was due to the intrinsic properties of the SnS_2 nanoflakes, rather than on the contact state or device properties. The photoresponse times of the mesa-shaped SnS_2 nanoflakes developed in this study and those of previously reported regular SnS_2 nanoflakes are listed in Table S1 (in the ESM). Compared with the other SnS_2 nanoflakes, the mesa-shaped SnS_2 nanoflakes exhibit a comparable or shorter photoresponse time. We demonstrated a feasible and simplified method for determining the photoresponse times of 2D materials using photoconductive AFM, avoiding complicated photolithography and electrode-deposition procedures.

According to previous reports, many 2D materials with optimal electrical and photoelectrical properties are not single-layered but are several nanometers to dozens of nanometers thick [76–78]. Therefore, to study the relationship between the photoresponse time and the thickness of the SnS_2 nanoflakes, we investigated the thickness-dependent photoresponse properties of SnS_2 nanoflakes for the first time by using photoconductive AFM. A series of photoconductive AFM experiments was performed on the top platforms of more than 200 mesa-like SnS_2 nanoflakes with a broad range of thicknesses under the same conditions. The statistical data for the thickness-dependent photoresponse time are summarized in Figs. 5(i) and 5(j). As the thickness increased from 1.0 to ~20 nm, both T_r and T_d decreased rapidly. With the further increase of the thickness, T_r and T_d remained in a roughly stable range: approximately 17–90 ms (~67 ms on average) for T_r and 10–55 ms (~30 ms on average) for T_d. This result is comparable to the photoresponse time of other SnS_2 materials reported in the literature [30, 33]. The fluctuation of the photoresponse time is attributed to the charged impurities or trap states at the interface between the nanoflake and the substrate. We also compared the photoresponse performance of the SnS_2 nanoflakes with that of previously reported 2D materials, as shown in Table S2 (in the ESM). The typical T_r and T_d of the SnS_2 nanoflakes (17 and 35 ms, respectively) are comparable to or better than those of the other materials. The fast and notable photoresponse shows the potential of the mesa-shaped SnS_2 nanoflakes for applications in photodetectors and other photoelectric devices.

4 Conclusions

Mesa-shaped hexagonal SnS_2 nanoflakes with monolayer atomic steps were successfully grown via APCVD by using SnS and sulfur as precursors. A layer-wise epitaxial growth mechanism was proposed to explain the growth process. *In situ* AFM measurements and Raman characterizations directly reflected the evolution of the A_{1g} peak intensity and Raman shifts with respect to the thickness of the SnS_2 nanoflakes. Photoconductive AFM measurements of the mesa-like SnS_2 nanoflakes revealed the different photoconductive behaviors of the edges and the flat surfaces of the monolayer atomic steps. The photoresponse time of the SnS_2 nanoflakes was strongly dependent on the thickness. We expect that the mesa-like SnS_2 nanoflakes with monolayer atomic steps and special optoelectronic properties can be applied in high-performance photodetectors and next-generation quantum devices.

Acknowledgements

We thank Prof. Qian Yu at Zhejiang University for the help in the aspect of high-resolution TEM characterizations. This work is supported by National Basic Research Program of China (No. 2015CB659300), National Materials Genome Project (No. 2016YFB0700600), National Natural Science Foundation of China (Nos. 21403105 and 21573108), China Postdoctoral Science Foundation (Nos. 2015M580408, 2015M581775, 2015M580413 and 2015M581769), Natural Science Foundation of Jiangsu Province (Nos. BK20150571 and BK20160647), Fundamental Research Funds for the Central Universities and a project funded by the Priority Academic Program Development (PAPD) of Jiangsu Higher Education Institutions.

Electronic Supplementary Material: Supplementary material (comparison of photoresponse times of mesa-shaped SnS_2 nanoflakes in this study with previously-reported regular SnS_2 crystals and other 2D atomic crystals; optical microscopy characterizations; XRD characterizations; additional AFM images; high-resolution TEM characterizations; Raman peak area and FWHM of A_{1g} mode as the functions of thickness; topographic AFM and photoconductive *I*–*V* charac-

terizations of a SnS_2 nanoflake with a thickness of 75 nm; tip location and deflection setpoint vs. photoresponse time of a SnS_2 nanoflake with a thickness of 30 nm) is available in the online version of this article at http://dx.doi.org/10.1007/s12274-017-1525-3.

References

[1] Novoselov, K. S.; Geim, A. K.; Morozov, S. V.; Jiang, D.; Zhang, Y.; Dubonos, S. A.; Grigorieva, I. V.; Firsov, A. A. Electric field effect in atomically thin carbon films. *Science* **2004**, *306*, 666–669.

[2] Hashimoto, A.; Suenaga, K.; Gloter, A.; Urita, K.; Iijima, S. Direct evidence for atomic defects in graphene layers. *Nature* **2004**, *430*, 870–873.

[3] Kim, K. S.; Zhao, Y.; Jang, H.; Lee, S. Y.; Kim, J. M.; Kim, K. S.; Ahn, J.-H.; Kim, P.; Choi, J.-Y.; Hong, B. H. Large-scale pattern growth of graphene films for stretchable transparent electrodes. *Nature* **2009**, *457*, 706–710.

[4] Geim, A. K.; Novoselov, K. S. The rise of graphene. *Nat. Mater.* **2007**, *6*, 183–191.

[5] Novoselov, K. S.; Geim, A. K.; Morozov, S. V.; Jiang, D.; Katsnelson, M. I.; Grigorieva, I. V.; Dubonos, S. V.; Firsov, A. A. Two-dimensional gas of massless Dirac fermions in graphene. *Nature* **2005**, *438*, 197–200.

[6] Zhang, Y. B.; Tan, Y. W.; Stormer, H. L.; Kim, P. Experimental observation of the quantum hall effect and Berry's phase in graphene. *Nature* **2005**, *438*, 201–204.

[7] Li, X. S.; Cai, W. W.; An, J.; Kim, S.; Nah, J.; Yang, D. X.; Piner, R.; Velamakanni, A.; Jung, I.; Tutuc, E. et al. Large-area synthesis of high-quality and uniform graphene films on copper foils. *Science* **2009**, *324*, 1312–1314.

[8] Mas-Ballesté, R.; Gómez-Navarro, C.; Gómez-Herrero, J.; Zamora, F. 2D materials: To graphene and beyond. *Nanoscale* **2011**, *3*, 20–30.

[9] Butler, S. Z.; Hollen, S. M.; Cao, L. Y.; Cui, Y.; Gupta, J. A.; Gutiérrez, H. R.; Heinz, T. F.; Hong, S. S.; Huang, J. X.; Ismach, A. F. et al. Progress, challenges, and opportunities in two-dimensional materials beyond graphene. *ACS Nano* **2013**, *7*, 2898–2926.

[10] Radisavljevic, B.; Radenovic, A.; Brivio, J.; Giacometti, V.; Kis, A. Single-layer MoS_2 transistors. *Nat. Nanotechnol.* **2011**, *6*, 147–150.

[11] van der Zande, A. M.; Huang, P. Y.; Chenet, D. A.; Berkelbach, T. C.; You, Y. M.; Lee, G.-H.; Heinz, T. F.; Reichman, D. R.; Muller, D. A.; Hone, J. C. Grains and grain boundaries in highly crystalline monolayer molybdenum disulphide. *Nat. Mater.* **2013**, *12*, 554–561.

[12] Mak, K. F.; Lee, C.; Hone, J.; Shan, J.; Heinz, T. F. Atomically thin MoS_2: A new direct-gap semiconductor. *Phys. Rev. Lett.* **2010**, *105*, 136805.

[13] Mak, K. F.; He, K. L.; Shan, J.; Heinz, T. F. Control of valley polarization in monolayer MoS_2 by optical helicity. *Nat. Nanotechnol.* **2012**, *7*, 494–498.

[14] Splendiani, A.; Sun, L.; Zhang, Y. B.; Li, T. S.; Kim, J.; Chim, C.-Y.; Galli, G.; Wang, F. Emerging photoluminescence in monolayer MoS_2. *Nano Lett.* **2010**, *10*, 1271–1275.

[15] Li, H.; Wu, J.; Yin, Z. Y.; Zhang, H. Preparation and applications of mechanically exfoliated single-layer and multilayer MoS_2 and WSe_2 nanosheets. *Acc. Chem. Res.* **2014**, *47*, 1067–1075.

[16] Lee, Y. H.; Zhang, X. Q.; Zhang, W. J.; Chang, M. T.; Lin, C. T.; Chang, K. D.; Yu, Y. C.; Wang, J. T. W.; Chang, C. S.; Li, L. J. et al. Synthesis of large-area MoS_2 atomic layers with chemical vapor deposition. *Adv. Mater.* **2012**, *24*, 2320–2325.

[17] Zhang, Y.; Chang, T. R.; Zhou, B.; Cui, Y. T.; Yan, H.; Liu, Z. K.; Schmitt, F.; Lee, J.; Moore, R.; Chen, Y. L. et al. Direct observation of the transition from indirect to direct bandgap in atomically thin epitaxial $MoSe_2$. *Nat. Nanotechnol.* **2014**, *9*, 111–115.

[18] Ross, J. S.; Wu, S. F.; Yu, H. Y.; Ghimire, N. J.; Jones, A. M.; Aivazian, G.; Yan, J. Q.; Mandrus, D. G.; Xiao, D.; Yao, W. et al. Electrical control of neutral and charged excitons in a monolayer semiconductor. *Nat. Commun.* **2013**, *4*, 1474.

[19] Voiry, D.; Yamaguchi, H.; Li, J. W.; Silva, R.; Alves, D. C. B.; Fujita, T.; Chen, M. W.; Asefa, T.; Shenoy, V. B.; Eda, G. et al. Enhanced catalytic activity in strained chemically exfoliated WS_2 nanosheets for hydrogen evolution. *Nat. Mater.* **2013**, *12*, 850–855.

[20] Hong, X. P.; Kim, J.; Shi, S.-F.; Zhang, Y.; Jin, C. H.; Sun, Y. H.; Tongay, S.; Wu, J. Q.; Zhang, Y. F.; Wang, F. Ultrafast charge transfer in atomically thin MoS_2/WS_2 heterostructures. *Nat. Nanotechnol.* **2014**, *9*, 682–686.

[21] Late, D. J.; Liu, B.; Luo, J. J.; Yan, A. M.; Matte, H. S. S. R.; Grayson, M.; Rao, C. N. R.; Dravid, V. P. GaS and GaSe ultrathin layer transistors. *Adv. Mater.* **2012**, *24*, 3549–3554.

[22] Hu, P. A.; Wang, L. F.; Yoon, M.; Zhang, J.; Feng, W.; Wang, X. N.; Wen, Z. Z.; Idrobo, J. C.; Miyamoto, Y.; Geohegan, D. B. et al. Highly responsive ultrathin GaS nanosheet photodetectors on rigid and flexible substrates. *Nano Lett.* **2013**, *13*, 1649–1654.

[23] Park, K. H.; Jang, K.; Son, S. U. Synthesis, optical properties, and self-assembly of ultrathin hexagonal In_2S_3 nanoplates. *Angew. Chem., Int. Ed.* **2006**, *45*, 4608–4612.

[24] Zhou, J. D.; Zeng, Q. S.; Lv, D. H.; Sun, L. F.; Niu, L.; Fu, W.; Liu, F. C.; Shen, Z. X.; Jin, C. H.; Liu, Z. Controlled synthesis of high-quality monolayered α-In_2Se_3 via physical

vapor deposition. *Nano Lett.* **2015**, *15*, 6400–6405.

[25] Zhou, X.; Gan, L.; Tian, W. M.; Zhang, Q.; Jin, S. Y.; Li, H. Q.; Bando, Y.; Golberg, D.; Zhai, T. Y. Ultrathin $SnSe_2$ flakes grown by chemical vapor deposition for high-performance photodetectors. *Adv. Mater.* **2015**, *27*, 8035–8041.

[26] Hsieh, D.; Xia, Y.; Qian, D.; Wray, L.; Meier, F.; Dil, J. H.; Osterwalder, J.; Patthey, L.; Fedorov, A. V.; Lin, H. et al. Observation of time-reversal-protected single-Dirac-cone topological-insulator states in Bi_2Te_3 and Sb_2Te_3. *Phys. Rev. Lett.* **2009**, *103*, 146401.

[27] Zhang, Y.; He, K.; Chang, C. Z.; Song, C. L.; Wang, L. L.; Chen, X.; Jia, J. F.; Fang, Z.; Dai, X.; Shan, W. Y. et al. Crossover of the three-dimensional topological insulator Bi_2Se_3 to the two-dimensional limit. *Nat. Phys.* **2010**, *6*, 584–588.

[28] Zhang, H. J.; Liu, C. X.; Qi, X. L.; Dai, X.; Fang, Z.; Zhang, S. C. Topological insulators in Bi_2Se_3, Bi_2Te_3 and Sb_2Te_3 with a single Dirac cone on the surface. *Nat. Phys.* **2009**, *5*, 438–442.

[29] Su, G. X.; Hadjiev, V. G.; Loya, P. E.; Zhang, J.; Lei, S. D.; Maharjan, S.; Dong, P.; Ajayan, P. M.; Lou, J.; Peng, H. B. Chemical vapor deposition of thin crystals of layered semiconductor SnS_2 for fast photodetection application. *Nano Lett.* **2015**, *15*, 506–513.

[30] Huang, Y.; Sutter, E.; Sadowski, J. T.; Cotlet, M.; Monti, O. L. A.; Racke, D. A.; Neupane, M. R.; Wickramaratne, D.; Lake, R. K.; Parkinson, B. A. et al. Tin disulfide—An emerging layered metal dichalcogenide semiconductor: Materials properties and device characteristics. *ACS Nano* **2014**, *8*, 10743–10755.

[31] Sun, Y. F.; Cheng, H.; Gao, S.; Sun, Z. H.; Liu, Q. H.; Liu, Q.; Lei, F. C.; Yao, T.; He, J. F.; Wei, S. Q. et al. Freestanding tin disulfide single-layers realizing efficient visible-light water splitting. *Angew. Chem., Int. Ed.* **2012**, *51*, 8727–8731.

[32] De, D.; Manongdo, J.; See, S.; Zhang, V.; Guloy, A.; Peng, H. High on/off ratio field effect transistors based on exfoliated crystalline SnS_2 nano-membranes. *Nanotechnology* **2013**, *24*, 025202.

[33] Xia, J.; Zhu, D. D.; Wang, L.; Huang, B.; Huang, X.; Meng, X. M. Large-scale growth of two-dimensional SnS_2 crystals driven by screw dislocations and application to photodetectors. *Adv. Funct. Mater.* **2015**, *25*, 4255–4261.

[34] Ahn, J. H.; Lee, M. J.; Heo, H.; Ji, H. S.; Kim, K.; Hwang, H.; Jo, M. H. Deterministic two-dimensional polymorphism growth of hexagonal n-type SnS_2 and orthorhombic p-type SnS crystals. Nano *Lett.* **2015**, *15*, 3703–3708.

[35] Weast, R. C.; Astle, M. J.; Beyer, W. H. *CRC Handbook of Chemistry and Physics*; CRC Press: Boca Raton, FL, 1988.

[36] Mutlu, Z.; Wu, R. J.; Wickramaratne, D.; Shahrezaei, S.; Liu, C.; Temiz, S.; Patalano, A.; Ozkan, M.; Lake, R. K.; Mkhoyan, K. A. et al. Phase engineering of 2D tin sulfides. *Small* **2016**, *12*, 2998–3004.

[37] Park, J. C.; Lee, K. R.; Heo, H.; Kwon, S. H.; Kwon, J. D.; Lee, M. J.; Jeon, W.; Jeong, S. J.; Ahn, J. H. Vapor transport synthesis of two-dimensional SnS_2 nanocrystals using a SnS_2 precursor obtained from the sulfurization of SnO_2. *Cryst. Growth Des.* **2016**, *16*, 3884–3889.

[38] Samad, L.; Bladow, S. M.; Ding, Q.; Zhuo, J. Q.; Jacobberger, R. M.; Arnold, M. S.; Jin, S. Layer-controlled chemical vapor deposition growth of MoS_2 vertical heterostructures via van der Waals epitaxy. *ACS Nano* **2016**, *10*, 7039–7046.

[39] Zhang, X. W.; Meng, F.; Christianson, J. R.; Arroyo-Torres, C.; Lukowski, M. A.; Liang, D.; Schmidt, J. R.; Jin, S. Vertical heterostructures of layered metal chalcogenides by van der Waals epitaxy. *Nano Lett.* **2014**, *14*, 3047–3054.

[40] Wang, Q. S.; Xu, K.; Wang, Z. X.; Wang, F.; Huang, Y.; Safdar, M.; Zhan, X. Y.; Wang, F. M.; Cheng, Z. Z.; He, J. Van der Waals epitaxial ultrathin two-dimensional nonlayered semiconductor for highly efficient flexible optoelectronic devices. *Nano Lett.* **2015**, *15*, 1183–1189.

[41] Massa, W. *Crystal Structure Determination*; Springer: Berlin Heidelberg, 2013.

[42] Al-Alamy, F. A. S.; Balchin, A. A. The growth by iodine vapour transport and the crystal structures of layer compounds in the series SnS_xSe_{2-x} ($0 \le x \le 2$), $Sn_xZr_{1-x}Se_2$ ($0 \le x \le 1$), and TaS_xSe_{2-x} ($0 \le x \le 2$). *J. Cryst. Growth* **1977**, *38*, 221–232.

[43] Smith, A. J.; Meek, P. E.; Liang, W. Y. Raman scattering studies of SnS_2 and $SnSe_2$. *J. Phys. C* **1977**, *10*, 1321.

[44] Chhowalla, M.; Shin, H. S.; Eda, G.; Li, L. J.; Loh, K. P.; Zhang, H. The chemistry of two-dimensional layered transition metal dichalcogenide nanosheets. *Nat. Chem.* **2013**, *5*, 263–275.

[45] Lin, M.; Wu, D.; Zhou, Y.; Huang, W.; Jiang, W.; Zheng, W. S.; Zhao, S. L.; Jin, C. H.; Guo, Y. F.; Peng, H. L. et al. Controlled growth of atomically thin In_2Se_3 flakes by van der Waals epitaxy. *J. Am. Chem. Soc.* **2013**, *135*, 13274–13277.

[46] Cha, J. J.; Kong, D. S.; Hong, S.-S.; Analytis, J. G.; Lai, K. J.; Cui, Y. Weak antilocalization in $Bi_2(Se_xTe_{1-x})_3$ nanoribbons and nanoplates. *Nano Lett.* **2012**, *12*, 1107–1111.

[47] Kong, D. S.; Dang, W. H.; Cha, J. J.; Li, H.; Meister, S.; Peng, H. L.; Liu, Z. F.; Cui, Y. Few-layer nanoplates of Bi_2Se_3 and Bi_2Te_3 with highly tunable chemical potential. *Nano Lett.* **2010**, *10*, 2245–2250.

[48] Kong, D. S.; Koski, K. J.; Cha, J. J.; Hong, S. S.; Cui, Y. Ambipolar field effect in Sb-doped Bi_2Se_3 nanoplates by solvothermal synthesis. *Nano Lett.* **2013**, *13*, 632–636.

[49] Zhang, K. H.; Feng, S. M.; Wang, J. J.; Azcatl, A.; Lu, N.;

Addou, R.; Wang, N.; Zhou, C. J.; Lerach, J.; Bojan, V. et al. Manganese doping of monolayer MoS_2: The substrate is critical. *Nano Lett.* **2015**, *15*, 6586–6591.

[50] Nemes-Incze, P.; Osváth, Z.; Kamarás, K.; Biró, L. P. Anomalies in thickness measurements of graphene and few layer graphite crystals by tapping mode atomic force microscopy. *Carbon* **2008**, *46*, 1435–1442.

[51] Ji, Q. Q.; Zhang, Y. F.; Gao, T.; Zhang, Y.; Ma, D. L.; Liu, M. X.; Chen, Y. B.; Qiao, X. F.; Tan, P.-H.; Kan, M. et al. Epitaxial monolayer MoS_2 on mica with novel photoluminescence. *Nano Lett.* **2013**, *13*, 3870–3877.

[52] Wagner, R. S.; Ellis, W. C. Vapor-liquid-solid mechanism of single crystal growth. *Appl. Phys. Lett.* **1964**, *4*, 89–90.

[53] Huang, M. H.; Wu, Y.; Feick, H.; Tran, N.; Weber, E.; Yang, P. Catalytic growth of zinc oxide nanowires by vapor transport. *Adv. Mater.* **2001**, *13*, 113–116.

[54] Yan, A. M.; Velasco, J., Jr.; Kahn, S.; Watanabe, K.; Taniguchi, T.; Wang, F.; Crommie, M. F.; Zettl, A. Direct growth of single- and few-layer MoS_2 on h-BN with preferred relative rotation angles. *Nano Lett.* **2015**, *15*, 6324–6331.

[55] Hansen, L. P.; Johnson, E.; Brorson, M.; Helveg, S. Growth mechanism for single-and multi-layer MoS_2 nanocrystals. *J. Phys. Chem. C* **2014**, *118*, 22768–22773.

[56] Markov, I. V. *Crystal Growth for Beginners: Fundamentals of Nucleation, Crystal Growth and Epitaxy*; World Scientific Publishing Company: Singapore, 2003.

[57] Li, H.; Zhang, Q.; Yap, C. C. R.; Tay, B. K.; Edwin, T. H. T.; Olivier, A.; Baillargeat, D. From bulk to monolayer MoS_2: Evolution of Raman scattering. *Adv. Funct. Mater.* **2012**, *22*, 1385–1390.

[58] Wieting, T. J.; Verble, J. L. Interlayer bonding and the lattice vibrations of β-GaSe. *Phys. Rev. B* **1972**, *5*, 1473–1479.

[59] Lee, C.; Yan, H. G.; Brus, L. E.; Heinz, T. F.; Hone, J.; Ryu, S. Anomalous lattice vibrations of single- and few-layer MoS_2. *ACS Nano* **2010**, *4*, 2695–2700.

[60] Lucovsky, G.; Mikkelsen, J. C., Jr.; Liang, W. Y.; White, R. M.; Martin, R. M. Optical phonon anisotropies in the layer crystals SnS_2 and $SnSe_2$. *Phys. Rev. B* **1976**, *14*, 1663–1669.

[61] Mead, D. G.; Irwin, J. C. Raman spectra of SnS_2 and $SnSe_2$. *Solid State Commun.* **1976**, *20*, 885–887.

[62] Yu, H. Y.; Feng, X. D.; Grozea, D.; Lu, Z. H.; Sodhi, R. N. S.; Hor, A. M.; Aziz, H. Surface electronic structure of plasma-treated indium tin oxides. *Appl. Phys. Lett.* **2001**, *78*, 2595–2597.

[63] Hamberg, I.; Granqvist, C. G. Evaporated Sn-doped In_2O_3 films: Basic optical properties and applications to energy-efficient windows. *J. Appl. Phys.* **1986**, *60*, R123–R160.

[64] Singh, R.; Rajkanan, K.; Brodie, D. E.; Morgan, J. H. Optimization of oxide-semiconductor/base-semiconductor solar cells. *IEEE Trans. Electron Dev.* **1980**, *27*, 656–662.

[65] Son, Y.; Wang, Q. H.; Paulson, J. A.; Shih, C. J.; Rajan, A. G.; Tvrdy, K.; Kim, S.; Alfeeli, B.; Braatz, R. D.; Strano, M. S. Layer number dependence of MoS_2 photoconductivity using photocurrent spectral atomic force microscopic imaging. *ACS Nano* **2015**, *9*, 2843–2855.

[66] Son, Y.; Li, M. Y.; Cheng, C. C.; Wei, K. H.; Liu, P. W.; Wang, Q. H.; Li, L. J.; Strano, M. S. Observation of switchable photoresponse of a monolayer WSe_2-MoS_2 lateral heterostructure via photocurrent spectral atomic force microscopic imaging. *Nano Lett.* **2016**, *16*, 3571–3577.

[67] Freitag, M.; Low, T.; Xia, F. N.; Avouris, P. Photoconductivity of biased graphene. *Nat. Photonics* **2012**, *7*, 53–59.

[68] Lee, M. J.; Ahn, J. H.; Sung, J. H.; Heo, H.; Jeon, S. G.; Lee, W.; Song, J. Y.; Hong, K. H.; Choi, B.; Lee, S. H. et al. Thermoelectric materials by using two-dimensional materials with negative correlation between electrical and thermal conductivity. *Nat. Commun.* **2016**, *7*, 12011.

[69] Rhoderick, E. H. Metal-semiconductor contacts. *IEE Proc. I: Solid-State Electron Dev.* **1982**, *129*, 1.

[70] Klaua, M.; Ullmann, D.; Barthel, J.; Wulfhekel, W.; Kirschner, J.; Urban, R.; Monchesky, T. L.; Enders, A.; Cochran, J. F.; Heinrich, B. Growth, structure, electronic, and magnetic properties of MgO/Fe(001) bilayers and Fe/MgO/Fe(001) trilayers. *Phys. Rev. B* **2001**, *64*, 134411.

[71] Yu, Y.; Schoonen, M. A. A. The absolute energy positions of conduction and valence bands of selected semiconducting minerals. *Am. Mineral.* **2000**, *85*, 543–556.

[72] Zhang, Z.; Yates, J. T., Jr. Band bending in semiconductors: Chemical and physical consequences at surfaces and interfaces. *Chem. Rev.* **2012**, *112*, 5520–5551.

[73] Zangwill, A. *Physics at Surfaces*; Cambridge University Press: Cambridge, 1988.

[74] Cowley, A. M.; Sze, S. M. Surface states and barrier height of metal-semiconductor systems. *J. Appl. Phys.* **1965**, *36*, 3212–3220.

[75] Bardeen, J. Surface states and rectification at a metal semiconductor contact. *Phys. Rev.* **1947**, *71*, 717–727.

[76] Sui, Y.; Appenzeller, J. Screening and interlayer coupling in multilayer graphene field-effect transistors. *Nano Lett.* **2009**, *9*, 2973–2977.

[77] Das, S.; Chen, H.-Y.; Penumatcha, A. V.; Appenzeller, J. High performance multilayer MoS_2 transistors with scandium contacts. *Nano Lett.* **2013**, *13*, 100–105.

[78] Zhou, X.; Gan, L.; Tian, W. M.; Zhang, Q.; Jin, S. Y.; Li, H. Q.; Bando, Y.; Golberg, D.; Zhai, T. Y. Photodetectors: Ultrathin $SnSe_2$ flakes grown by chemical vapor deposition for high-performance photodetectors (Adv. Mater. 48/2015). Adv. *Mater.* **2015**, *27*, 8119.